Flow visualization and numerical analysis of a coflowing jet: a three-dimensional approach

By JUAN C. AGÜÍ AND LAMBERTUS HESSELINK

Department of Aeronautics and Astronautics, Stanford University, Stanford, CA 94305, USA

The instabilities of an acoustically excited coflowing jet are investigated by using a time series of cross-sections of large-scale structures present in the flow and by a fully three-dimensional numerical simulation via the vortex-element method. These structures are first revealed by a flow-visualization technique based on smoke seeding the inner jet flow and observing the flow cross-sections as the structures are convected past a stationary sheet of laser light. Usage of image-processing techniques along with computer graphics allows the full three-dimensional reconstruction of the structure. The general morphology of the flow is determined from the reconstructed views and shows that the vorticity is mainly concentrated into a single large-scale vortex ring. Hypotheses regarding the nature and origin of the longitudinal instabilities observed in the flow can be drawn from the reconstructed views, and are supported by the numerical simulations. Quantitative values such as the surface-to-volume ratio and the entrainment level are also obtained from the experimental data. The onset of streamwise vorticity and its distribution are derived from the numerical calculations as well. Three-dimensional views and a holographic display of a characteristic eddy are also presented.

1. Introduction

The objective of the present study is to investigate the structure of a coflowing air jet. This study is carried out in a fully three-dimensional manner using two different and complementary tools. The first one consists of a three-dimensional reconstruction of the flow from a smoke-visualization data base. The second is a numerical simulation of the jet by means of the vortex-element method. While the flow-visualization study shows the topology of the real flow in terms of a scalar added to the inner jet, the numerical simulation permits its analysis in terms of the vorticity distribution.

It is generally recognized that the increasing amount of available information from flow visualization of complex phenomena and/or computations is not being matched by our capability to analyse and understand all the information present in those data bases. The use of supercomputers which allow complex three-dimensional turbulent calculations to be carried out (frequently as a function of time) and the popularization of laser-sheet and two-dimensional laser-induced-fluorescence visualization are two clear examples of methods which today produce much more data than we can possibly assimilate.

One of the situations frequently encountered in fluid-mechanics research is the need to determine the structure of a fluid flow from a series of parallel cross-sections taken by optical means across its whole longitudinal span. In this context, Hesselink *et al.* (1983) applied the emission–absorption method (see §4) to the smoke-laden

wake behind a circular cylinder. With this method, they were able to address the cloud-within-a-cloud problem by using an adjustable degree of transparency. Although this method is suitable for high-contrast images, as encountered in medicine (stationary subjects) or liquid flows, its applicability to gaseous flows lacks the high contrast needed to discern internal structures that may be present in the interior of the flow. A new approach, combining image-processing techniques and computer graphics was first demonstrated by Jiménez, Bernal & Cogollos (1985), who applied it to the mixing region in a liquid mixing layer. Computer-graphics manipulation of the data allows the representation of hard surfaces that, although lacking any transparency, enable us to determine in a clearer way the structure of the marked flow. In the first part of this work, we discuss the reconstruction of a coflowing air jet. Its gaseous nature stresses the need for detailed and careful image processing. Higher diffusivity of smoke in air as well as generally lower Reynolds numbers yield, as a result, images in which the details of the inner structure are embedded in a low-contrast region. In the case of liquid mixing layers, on the other hand, the resulting images are often of high contrast.

The primary use of this technique is to generate three-dimensional views of the fluid objects. Internal cuts are also possible. Such images, which are much richer in information than their two-dimensional counterparts, prove to be of invaluable help in postulating the fluid-dynamic mechanisms underlying the observed features.

Furthermore, we show that quantitative results can be extracted from the three-dimensional flow-visualization data. Up to now, the type of numerical results obtained from flow-visualization data have been mostly local information representing densities, concentrations or velocities at a certain point in the flow. Equally interesting quantities are global parameters which describe the entire flow at once since, for example, they enable a global cross-comparison of the flow with other flows or theoretical models. Features of this sort are the entrainment ratio, the surface-to-volume ratio, and geometrical quantities such as syntactic descriptors of coherent eddies (González 1987; Hesselink & Helman 1987).

The structure of round jets and coflowing jets have been subjected through the years to many different explanations and hypotheses (Becker & Massaro 1968; Hussain & Clark 1981; Lau & Fisher 1975) the variety of which may largely be caused by the different experimental conditions and Reynolds numbers of each of the experiments. Nevertheless, most of the literature has concerned itself with the cylindrically symmetric aspects of the jet. The development of longitudinal (streamwise) instabilities normal to the main vortex ring, which form in most experiments and break the revolution symmetry of the flow, is not so well analysed or documented. These instabilities are of importance, since they may very well lead to the instability of the main vortex ring, and a subsequent turbulent breakup of the flow.

While the flow visualization provides an apparently detailed representation of the flow, the most accurate quantitative description will always be given in terms of flow variables, with vorticity being perhaps the most important one. In this context, a vortex-element method is used to model the flow and its time evolution. The success of this method of analysis has already been proved (Leonard 1985; Ashurst 1981) in modelling wakes, boundary layers and other vorticity governed flows. The results of these calculations, consisting essentially of spatial vorticity distributions, are frequently displayed in a quasi-three-dimensional skeletal form. These results are used to reinforce the hypotheses about the jet structure drawn from the flow-visualization images and reconstructions.

2. Original data

A round jet is issued inside a parallel stream of fluid at a slightly higher velocity than that of the outer stream. As a result of this configuration, a cylindrical vortex sheet forms at the interface between the jet and the outer stream. The sheet is unstable and tends to roll-up into vortices that are subsequently convected downstream along with the mean flow in which they are immersed. To lock-up that instability process, the jet is acoustically excited by means of a loudspeaker present in an upstream plenum chamber of the jet flow facility.

Owing to the excitation, the vortex rolling-up process occurs at the external frequency rate of 10 Hz and a single, isolated and well-defined quasi-periodic vortex ring is produced in each cycle.

The experimental apparatus is fully described in Strawa & Cantwell (1985). In this case, the Reynolds number based on the exit nozzle diameter (2.2 cm) and the jet velocity (50 cm/s) is approximately 2300. The Strouhal number is 0.44 and the excitation amounts to a modulation of up to 10 % of the mean jet speed. The tunnel is operated at pressure of 2.1 MPa over atmospheric to provide a higher Reynolds number. To visualize the resulting flow structure, the inner jet is seeded with kerosene smoke and a sheet of laser light of a thickness less than 1 mm is placed perpendicular to the jet direction 75 mm downstream from the nozzle, as shown in figure 1. As the resulting cylindrical vortex is convected downstream, the scattered light showing consecutive cross-sections is recorded on 16 mm movie film. The filming rate used is 400 f.p.s. and the number of cross-sections used to describe one cycle is 40. The movie frames are then projected onto a screen and digitized with an on-axis video camera connected to a VICOM image processor. Figure 2 shows four consecutive cross-sections corresponding to the highly rolled-up portion of the jet.

The resolution attained within the displayed cross-sections is a little better than 0.1 mm per pixel, while the time resolution between any consecutive cross-sections (2.5 ms) seems to be sufficient for a quite accurate description of the flow, since the variation from one cross-section to the next one turns out to be small.

It is clear that a Galilean transformation is implicitly assumed in converting the time in which a particular cross-section is convected through the laser sheet to its longitudinal position in the desired instantaneous portrait of the flow field as a whole. The constant of the transformation is clearly the convection velocity of the structure. The fidelity of the Galilean-transformed image with respect to the real one depends on the uniformity of the convection velocity and, mainly, on the degree of evolution that the structure undergoes in the time needed to completely convect past the stationary sheet of light.

For the case when the flow is found to be strictly repetitive, a phase-conditioned sampling would avoid the Galilean transformation. Experimentally, this can be achieved by scanning the visualizing laser sheet throughout the flow and by slaving the exposure time to the phase of the structure. However, though our flow is repetitive on a global scale, the phase-conditioned approach could not be applied here because the small-scale details are not fully repetitive and they would therefore loose coherence from one exposure to the next.

Following Cantwell (1981), it is possible to estimate the degree of evolution during the convection time of a large eddy past the stationary sheet of light. In an impulsive flow, the time evolution of spatial scales δ and velocities U is as follows:

$$\delta \sim M^{\frac{1}{4}}t^{\frac{1}{4}}, \quad U \sim M^{\frac{1}{4}}t^{\frac{1}{4}-1},$$
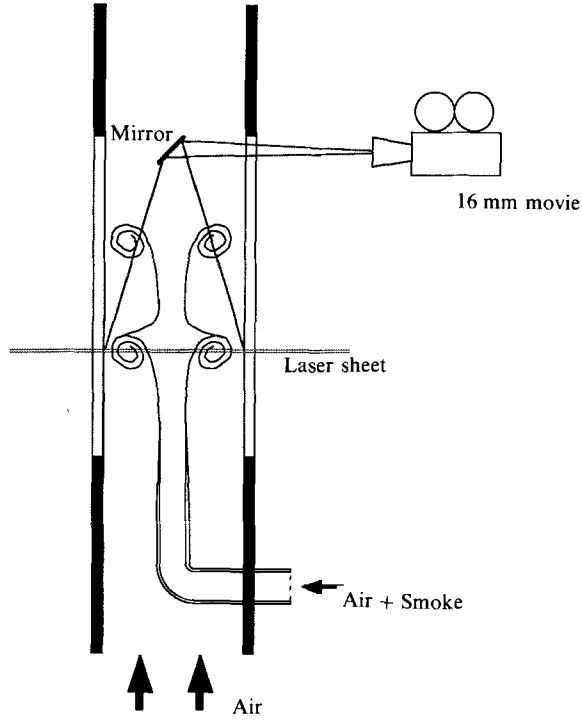
FIGURE 1. Experimental set-up. Visualization and recording arrangement.
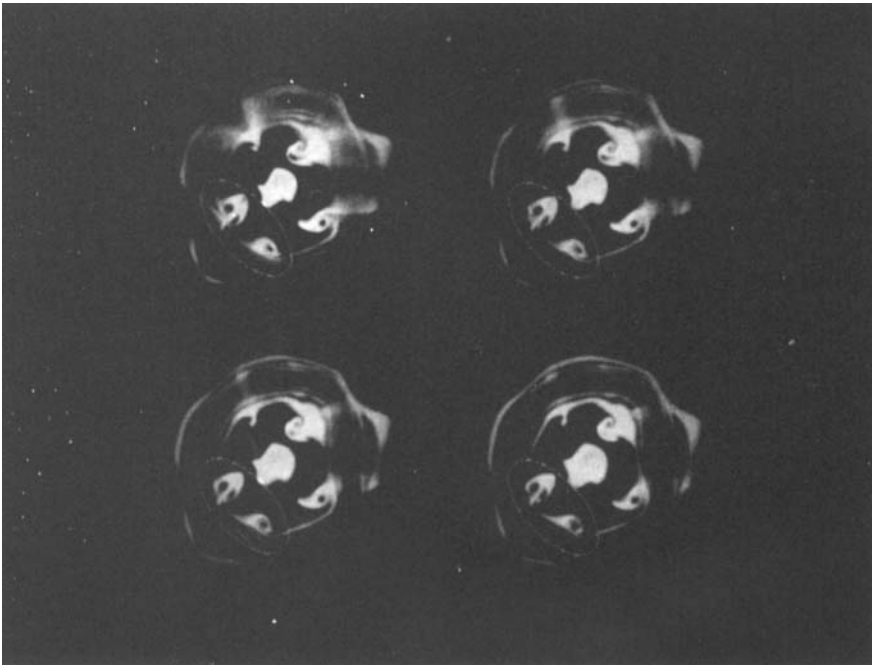
FIGURE 2. Four consecutive cross-sections of the coflowing jet. $x/\lambda = 0.575–0.65$. Time between frames is 2.5 ms.

where M is the integral constant of the flow, defined as

$$M = \left(\frac{I}{\rho}\right) = \frac{3}{2}\int U_x \, dV,$$

where ρ is the density and I is the impulse obtained by extending the integral to all the fluid volume that is convected pass the stationary light sheet during a full cycle of the jet instability. Log-differentiating the expression for δ we obtain, since M is constant,

$$\frac{\Delta\delta}{\delta} \approx \kappa\frac{\Delta t}{t},$$

and therefore, the time needed for an evolution $\Delta\delta \sim \delta$ is of order t/κ. In terms of the dimensions measured downstream from the nozzle, and using the above value for κ, we get

$$\Delta X_{evolution} \approx 4 \times X_{nozzle}.$$

Thus the desired ratio of the evolution time (or space) during the convection time (or longitudinal size) is as follows:

$$\frac{\Delta X_{evolution}}{\text{Longitudinal size}} \approx \frac{4 \times X_{nozzle}}{T \times U_{convection}}.$$

For a distance downstream of the nozzle of 75 mm and for the worst case of the convection velocity being equal to the jet velocity of 0.5 m/s and $T = \frac{1}{10}$ s the above ratio is 6, showing that the worst-case violation implied by using the Galilean transformation is about 16%.

The experimental work, including the image recording, was performed by R. Subbarao and B. Cantwell.

3. Digital image processing

Once the images are available in the computer in numerical form, the first task is to classify every point in the cross-sections as either 'smoke' or 'non-smoke' corresponding to fluid particles coming from the inner jet or the outer stream, respectively. We shall be using hereinafter the words 'smoke' and 'non-smoke' to identify the two pixel classes, as just described. In this process, smoke pixels are assigned a full white colour, while non-smoke ones are turned fully dark. This represents a first step in data compression, since the classified data has only two levels and can then be efficiently stored.

Performing that classification poses a great challenge when the goal is to keep the maximum available detail possible in the images while avoiding any amplification of noise. As pointed out in §1, owing to the high diffusivity of smoke in air, the fine detail of the inner structure of the rolling process is embedded in a low-contrast region of a rather high average luminosity, as shown in figure 3. Because of the large number of images to be processed, sophisticated and time-consuming segmentation algorithms were ruled out. Therefore, a contrast enhancement method followed by a thresholding operation were used, as described below.

The digital image processing of the cross-sections consists of three different steps. First, the images are cleaned from the background noise by an intensity thresholding, which preserves the values larger than a specified threshold while nulling all pixels under it. Secondly, a feature enhancement process is applied to the images to
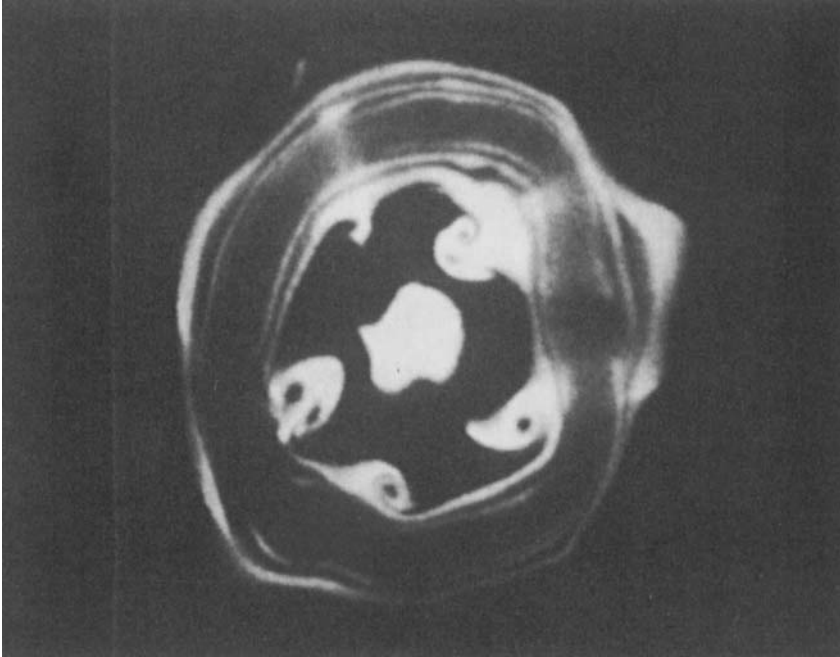
FIGURE 3. Original cross-section. $x/\lambda = 0.625$.

augment the flow characteristics (and possibly the remaining noise!) by subtracting the average base value in the neighbourhood of the pixel under consideration and a subsequent linear expansion to span the full dynamic range of 8 bits or 256 grey levels. This procedure is very similar to the well-known unsharp masking filtering, as described by Pratt (1978). Applying a thresholding algorithm to this feature-enhanced image is now enough to extract most of the information contained in it. The majority of the noise that may have leaked through the process is finally removed from the black-and-white image by means of a median filtering operation, as described in Pratt.

There is in this process a certain degree of subjectivity connected to the values selected as threshold, mainly those of the second thresholding operation. It is obvious that too low a threshold will give rise to smoke pixels that may be only slightly higher in intensity than their neighbouring outer-fluid pixels, essentially caused by noise effects alone. On the other hand, a threshold set too high will only recognize those portions of smoke fluid that are intensely bright, overlooking those that for some reason are slightly dimmer, but clearly belong to material coming from the inner jet. We have found through experimentation that variations of the threshold value on the order of 30% (which produce segmented images that are clearly far away from the expected result) may result in variations in the flow quantities of interest, like the surface-to-volume ratio, of up to a maximum of 20%.

The determination of the boundary between the two fluid regions is of the utmost importance since that boundary represents the interface between the two streams, that is to say, the region where the two fluids come into close contact and where truly molecular mixing takes place. In reacting flows, the reaction rate is proportional to, among other factors, the amount of interface area between the reactants, which is easily determined from the segmented images.
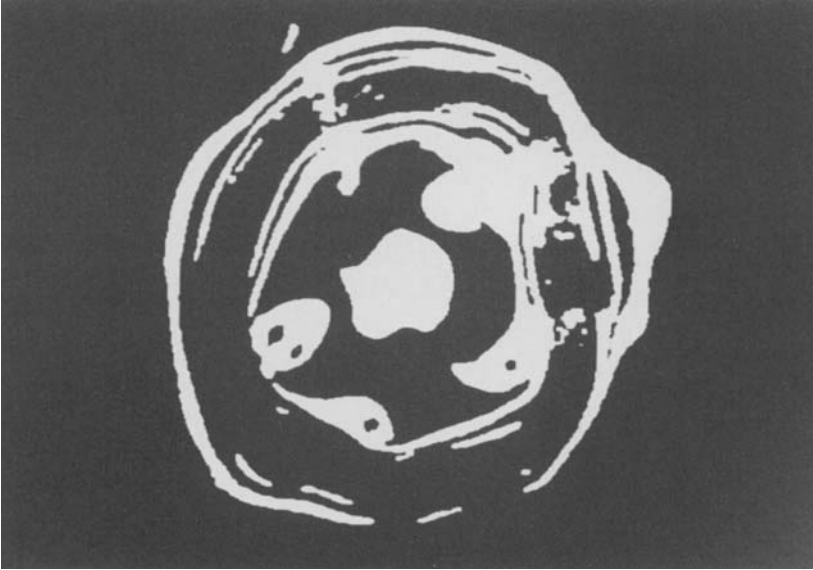
FIGURE 4. Two-level segmentation of the cross-section in figure 3. White areas correspond to smoke fluid from the inner jet.
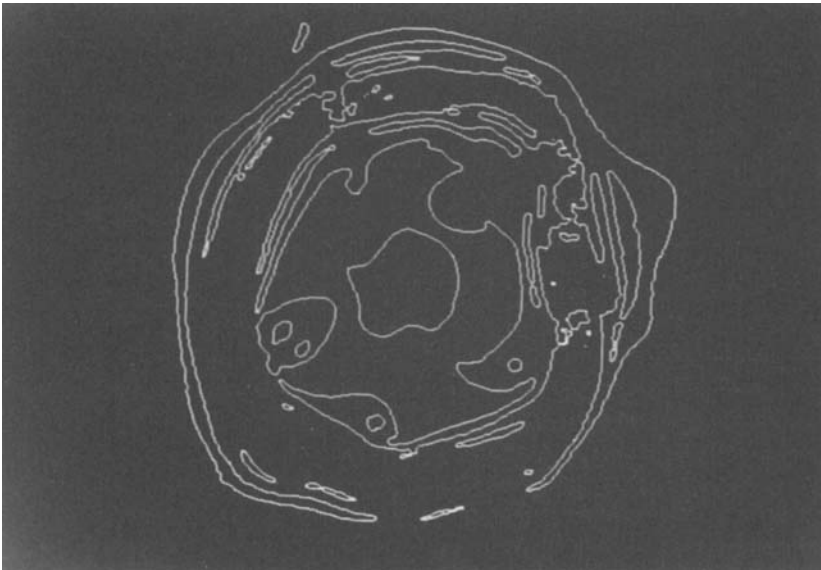
FIGURE 5. Interface between the inner jet and the outer stream, as obtained from the classified cross-section in figure 4.

The process is visualized in figures 3–5, using a typical cross-section. Figure 3 represents the original digitized image, figure 4 its classified version while figure 5 shows the boundary between the two fluids. The main difficulty that still persists is the fact that very strained portions of the inner jet fail to scatter enough light to be classified as smoke material. Consequently, parts of the jet may appear to be

unconnected even though the original image shows a faint smoke bridge between regions. Although morphological image processing and pattern-recognition procedures might be able to re-create those lost connections, it would always be attained at the risk of creating artifacts in the restored image and it was not attempted in the present study.

Most of the processing of the images has been carried out on a VICOM image processor connected to a VAX-11-780 computer.

4. Solid reconstruction and display techniques

The first objective of any modelling and/or display process is often to produce two-dimensional projections of a three-dimensional model of the described object, as a means for achieving full comprehension of its structure. The final goal is to display the spatial structure in three dimensions, thus allowing the observer to select his preferred perspective and showing essentially all the information available in the source data base. As will be shown later, holographic methods are capable and suitable for attaining the final goal of displaying the fluid structures.

The reconstruction of a solid out of a series of cross-sections can be done in several different ways. An emission–absorption procedure, as described in Hesselink *et al.* (1983), stacks all the cross-sections one after the other in an imaginary three-dimensional space. Each slice is previously replicated by the proper amount as computed from the filming rate and the convection velocity. Then, each voxel† behaves as a light emitter proportional to the amount of smoke originally present in that particular location in the set of images (i.e. light scattered and recorded on the film) and as an attenuator for the light emitted by pixels farther away from the viewer, as will be discussed in more detail in §8. The result is a view of a solid with an adjustable degree of transparency which allows the information that is usually hidden by the external surface of the structure to be seen. On the other hand it lacks important depth cues produced by effects such as shadows and lighting. The source-attenuation method is more suitable for high-contrast images such as those produced by liquid-fluorescence experiments, but if used with low-contrast images, or images with very fine detail, the results are somewhat fuzzy.

Another technique involves analysing each cross-section and reducing it to a set of closed singly or multiply connected polygons whose description is just an ordered list of points in a plane. In this manner, it is possible to undertake the analysis of the topological evolution from one cross-section to the next. This is, in the general case, an extremely difficult and costly task. If done, a smooth approximation to the real surface of the body is obtained which can then be represented in an opaque way (Jiménez 1985; Fuchs, Kedem & Uselton 1977).

Our approach is somewhere in between the two just described. The data (cross-sections) are not analysed in geometrical terms and each section is processed separately, thus eliminating the need for finding topological connections. This avoids any danger of loss of information and produces some savings in computer time. The process consists of creating a cylinder whose cross-section corresponds to our data and whose height is the spacing between slices. The three surfaces of this cylinder (front and rear planes plus the side surface) are then drawn using a z-buffer algorithm for hidden-surface removal (see Newman & Sproull 1979; or Foley 1983). Stacking those cylinders properly, a very convincing representation of the solid is achieved.

† Pixel in three-dimensions, or the minimum addressable volume unit.
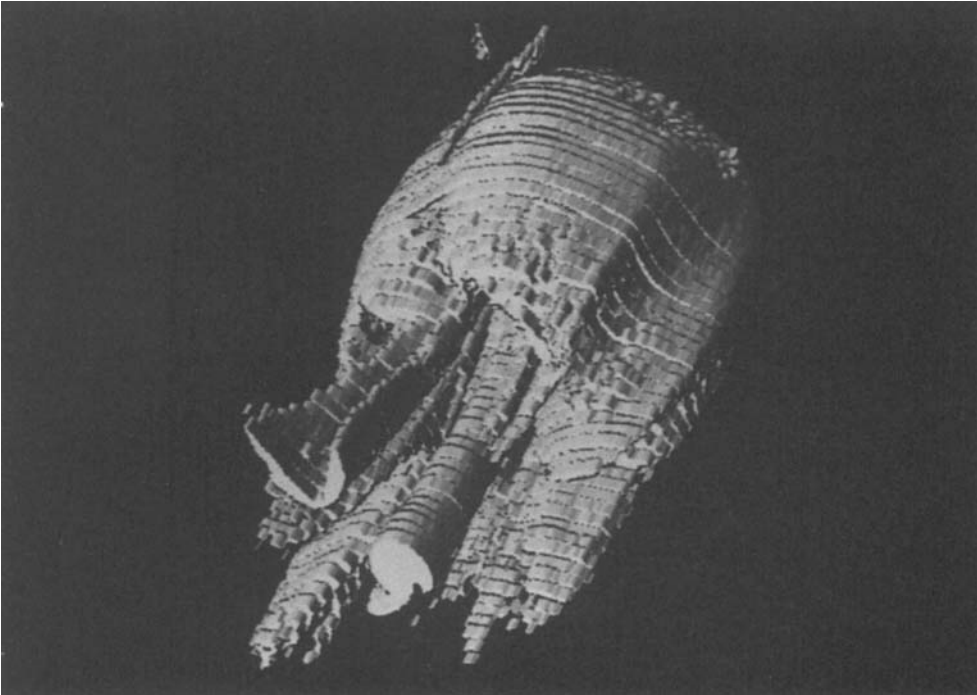
FIGURE 6. Perspective view of the coflowing-jet structure. Flow is from bottom left to top right.

The saved effort is redirected to a more flexible projection algorithm and towards a lighting scheme that improves the three-dimensional cues, as shown in figure 6. The drawback of this approach is that the evolution of the volume in between the slices is not described and a sometimes distracting 'staircase-look' results. In our particular study, however, a fraction of the discontinuity between the slices is caused by some misregistration of the film during the digitization process. On the other hand, a small amount of discontinuity between adjacent cylinders tends to enhance the stereo cues and improve depth perception. In addition, we have the ability of producing 'cuts' on the solid along any specified plane. In this way, the internal structure is easily visualized as shown in figures 7 and 8.

5. Qualitative results, topology

The results of our reconstruction algorithm are shown in figure 6. Here the rolled-up jet can be seen like a structure that has a well-defined dome-like front body as a result of the ring forming process, and a stem, or thinner trailing section corresponding to the unrolled portion of the jet. Several longitudinal structures also seem to emerge from the main body. Figures 7 and 8 are two different cuts of the structure, showing internal details of the vortex ring.

For a Reynolds number close to 2300 the observable mode of breakup essentially consists of the forming of well-defined vortex rings. The models shown in figures 6–8 essentially agree with the vortex-ring street as proposed by Lau & Fisher (1975), although in our case the periodicity and the spacing is fixed by the external excitation.
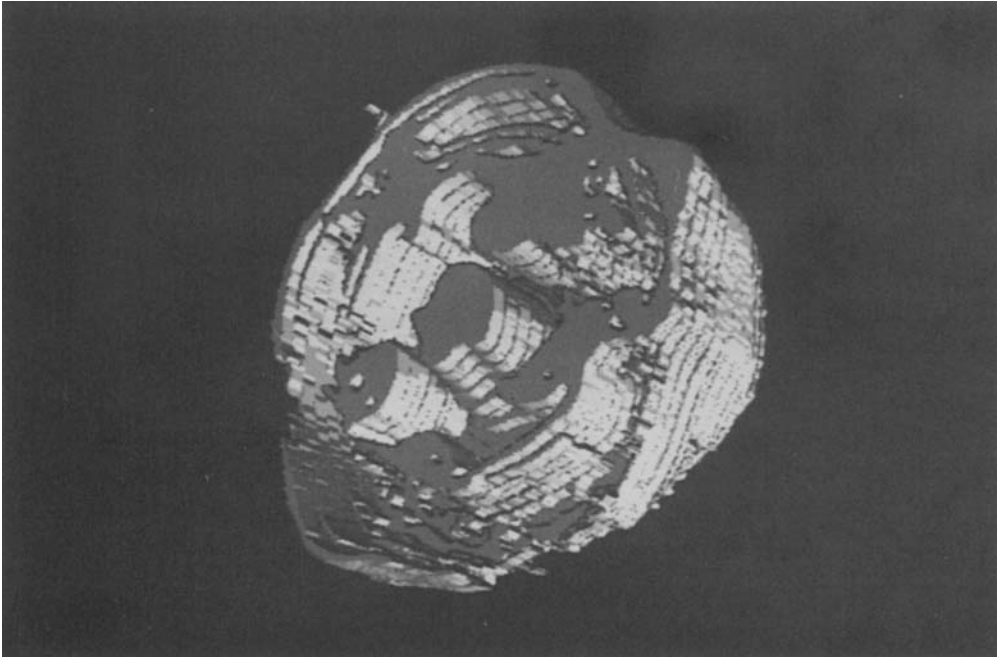
FIGURE 7. Normal cut of the coflowing-jet structure.
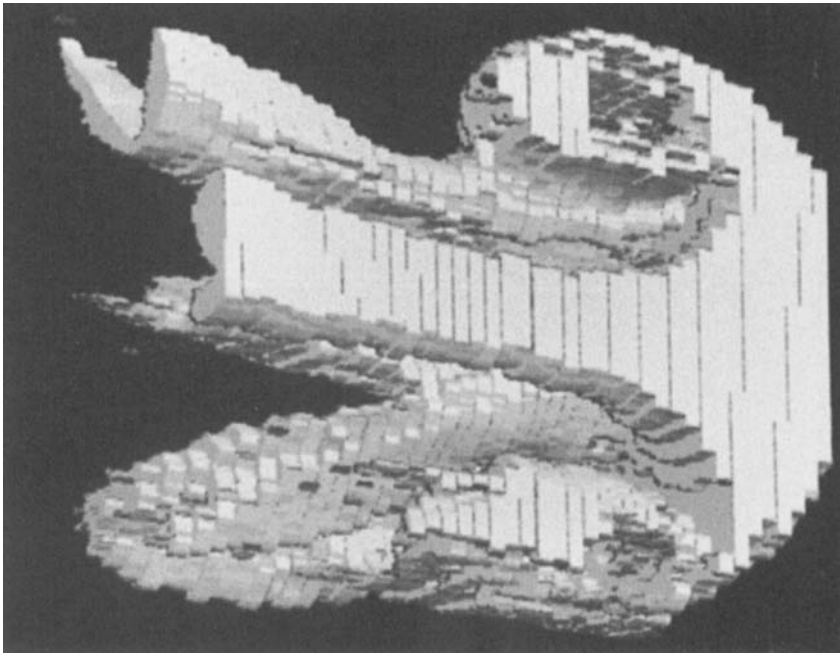
FIGURE 8. Longitudinal cut of the coflowing-jet structure.

Other experiments done by Perry, Lim & Chong (1980) using stroboscopic illumination on laterally vibrating jets or wakes show patterns that are somewhat similar to those presented here.

In accordance with Becker & Massaro (1968), there seem to be longitudinal structures which are shed from the main rolled-up forebody and then persist over a considerable downstream distance before they are entrained back into the jet itself. They postulated that these longitudinal structures are shot downstream. Our reconstructions show the shedding of longitudinal structures as well, though in our case they are shot upstream, rather than downstream, and they may correspond to a different mechanism. In figure 6, it is possible to discern up to six streamers trailing behind the main body. The central one obviously corresponds to the core of the jet which has been strongly stretched by the velocity field induced by the sequence of main vortex rings. The other five do not persist very far upstream except one, for which the remnant of the same longitudinal structure of the previous vortex ring is seen to lie outside the dome produced by the swollen main body of the roll-up. It is possible to connect these five structures with the five instabilities inside the vortex ring, which can be easily spotted in figure 3, a cross-section corresponding to the central part of the main body. Figure 8 shows a view of the whole eddy sliced along a longitudinal plane. It confirms the fact that both the external structures and the internal instabilities are just two manifestations of the same longitudinal instability.

Though the first reaction is to attribute the presence of these longitudinal structures to instabilities of the main vortex ring (see Widnall 1975), the cross-sections in figures 2 and 3 show that the longitudinal instabilities are well developed and cannot be interpreted as produced by instabilities of the main vortex ring, which remains, for the major part, unperturbed by the presence of the longitudinal structures. What the flow visualization suggests is that there is *longitudinal* vorticity *inside* the swollen body formed by the entrainment caused by the main vortex ring. These vorticity filaments appear frequently in counter-rotating pairs since each pair is most likely a loop or a hairpin vortex line which has been entrained and whose intensity has been amplified by the shear produced by the main vortex ring. These counter-rotating pairs are visualized by the smoke in figure 3 in the form of the internal mushroom-like vortices. The top end of the loops may or may not be engulfed inside the core of the main vortex ring. The faint bridges of smoke that can be seen in figure 3 inside the core of the vortex ring at the azimuthal positions corresponding to the longitudinal vortices suggest that, at the stage of evolution recorded in the current data, most, but not all, of the vortex-line loops have been partially entrained inside the main vortex ring core. Figure 8 shows that one of the longitudinal structures maintains its identity until it fuses with the top of the cavity filled with clear entrained fluid. Figure 9 features two views of one of the longitudinal structures cut out from the smoke pictures. In it, the vortex-line loop structure becomes more evident.

The sequence of papers by Corcos and co-workers (Corcos & Sherman 1984; Corcos & Lin 1984; Lin & Corcos 1984) on deterministic models for the mixing layer offer a quite complete picture of the evolution of a plane vorticity interface. Although their results apply to a plane mixing layer, the conclusions can be extrapolated to the coflowing jet which is formed by a closed cylindrical mixing layer. Similar to the plane mixing layer, the circumferential (spanwise) vorticity tends to aggregate into big recirculating lumps, which are connected by highly strained portions of the cylindrical interface (braids). It is at the locations of maximum strain where the circumferential vorticity becomes the most unstable and tends to align in the vertical
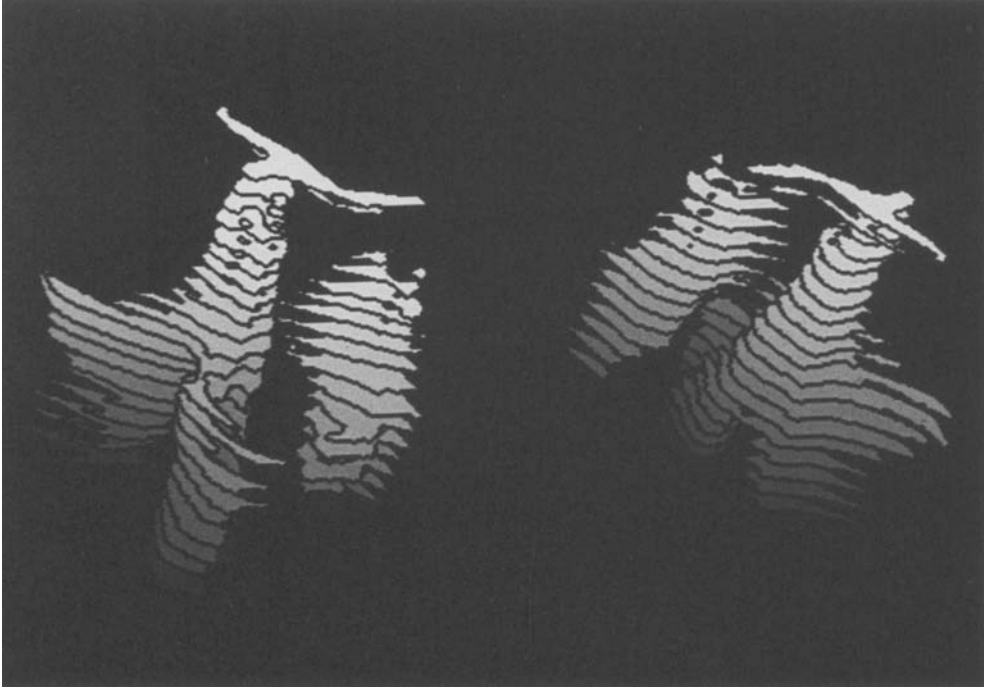
FIGURE 9. Cut out showing a longitudinal instability of the coflowing jet. Flow is from bottom up. The figure is assembled by simply stacking the portions of the slices corresponding to the features selected in figure 2. A varying shade and a black outline are included to improve the visibility of the slices. Left: external view looking inside. Right: view from the axis of the jet outwards. The top corresponds to the fusing of the structure with the top end of the entrained cavity.

direction (streamwise). Since the total vorticity along the mean direction has to remain constantly equal to zero, the longitudinal vorticity in the braids is composed of patches of alternating signs. The evolution of these patches and the effect on a passive-scalar interface is described in Lin & Corcos (1984). The resemblance between the patterns calculated by them and the internal cross-sections of the longitudinal structures in figure 3 is very significant.

Figure 6 shows how the remnant of one longitudinal structure shed from the previous period of the jet excitation seems to be stretched over the main body of the following one and is possibly entrained into it. At exactly the same place, a new longitudinal structure clearly emerges. This suggests a mechanism in which the instabilities are triggered from one period to the next one by means of these longitudinal long-lived structures. We believe that the origin of the longitudinal vorticity lies in the shear produced by the main vortex rings, although a small initial seed may be placed in the flow by the bend present upstream from the nozzle. Further experiments in a redesigned facility also exhibit the appearance of related four-to-five-fold instabilities without the presence of any significant initial longitudinal vorticity to trigger the instability pattern.

Figure 7 represents a normal cut along the main body showing its inside structure. It clearly shows the magnitude and extent of the instability of the vortex ring. Besides showing the longitudinal extent of the internal instabilities, it gives an idea of how much clear fluid has been entrained inside the rolled-up body (see §7 for further considerations on this last aspect). It finally shows that the thickness of the outer layer is far from being cylindrically homogeneous, although we believe that

gradients in the illumination procedure during the experiment may possibly be partially responsible for that non-uniformity.

6. Numerical simulation

In order to confirm the nature and origin of the streamwise vorticity present in the co-flowing jet, a simulation of a simplified flow has been carried out using the vortex-element method (Leonard 1985).

Assuming that the jet divergence is not an aspect of importance in the development of streamwise vorticity,† the periodic excited jet is modelled by an infinite cylindrical vorticity sheet, with a periodic modulation of the circulation intensity along the longitudinal axis. The distribution of circulation thus resembles the effect of the periodical acoustical excitation on the jet and locks the instability of the interface to the externally imposed wavelength. This tube of vorticity is discretized into a stack of vortex rings whose circulation is periodically modulated as a function of the ring initial position, and whose initial uniform spacing is on the order of the core diameter initially conferred to the rings. The rings are further discretized into segments which are subsequently treated as rectilinear elements as shown in figure 10(a). The central wavelength is the only one being considered and the others are simply replicated versions of it. Unfortunately, there is not a simple analytic result for the velocity induced by an infinite row of three-dimensional vortex segments, and a full numerical summation has to be performed for the determination of the velocity at each of the end-points of the segments that constitute the rings (typically 3200). This summation has to be carried out accurately in order to ensure the full periodicity that will avoid interference between the edges of the adjoining replicated wavelengths, which may result in undesirable edge effects.

The self-induced velocity in the vortex line can be given, in the slender regime ($\delta/l \ll 1$, where δ is the core size and l is a characteristic flow dimension) by using the cutoff approximation (Moore & Saffman 1972), as

$$u(r, t) = -\frac{\Gamma}{4\pi} \int_{|s-s'|>\epsilon} \frac{[r(s) - r'(s')] \times \frac{\partial r'}{\partial s'}}{|r(s) - r'(s')|^3} \, \mathrm{d}s',$$

where s and s' are the coordinate along the lines, and Γ is the circulation of the velocity-inducing vortex line. Leonard (1975) used the above expression for computing the evolution of a set of vortex lines described by rectilinear segments. The velocity at each of the nodes is given by a regular Biot–Savart term that includes the effect of all the segments not adjacent to the point under consideration plus a term that accounts for the local curvature of the line and the size of the core at that particular location. This last term represents the self-induced velocity and takes care of the singularity present in the Biot–Savart law by means of the cutoff integral, as shown above. Leonard's expressions are used in the current study.

Another necessary consideration relates to the evolution of the vortex core, which is the only point where the Reynolds number enters into play, in an otherwise effectively inviscid computation. The size of the vortex core is allowed to vary locally, even within the same vortex ring, under the effects of viscous diffusion and the influence of local stretching. However, as is required, the total circulation assigned to a vortex segment remains constant throughout the complete simulation. The desired Reynolds number simply fixes the value of the viscosity used.

† Which amounts to a *time*-developing study of a *spatially* growing flow.
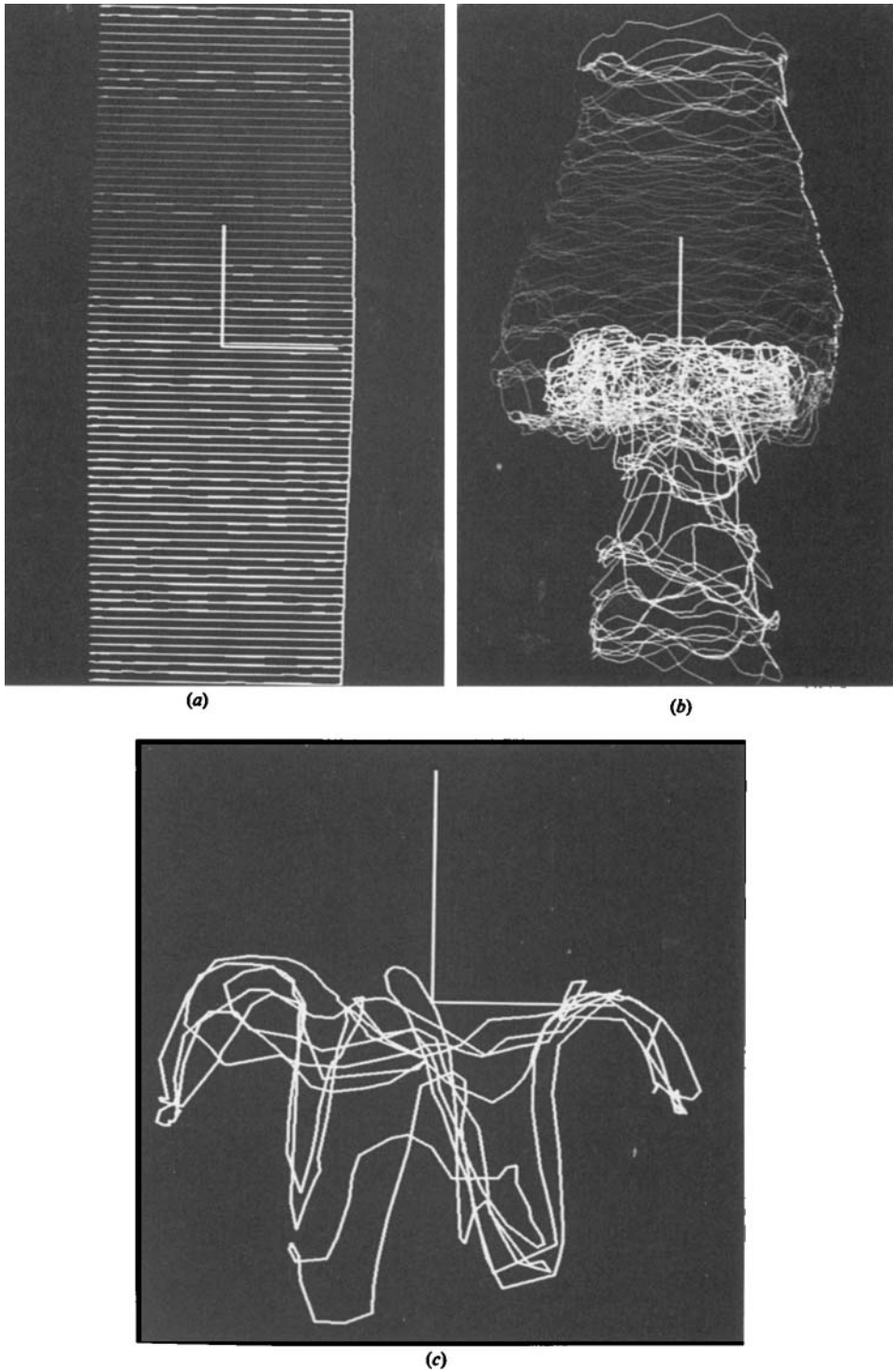
FIGURE 10. Numerical simulation of the coflowing jet. Only one wavelength of the infinite tube is displayed. Lines represent vortex filaments. Brightness is proportional to the circulation. Flow is vertical. (a) Early stage, $\tau = 0.8$, (b) $\tau = 3.2$, (c) selected rings from (b).

Furthermore, to maintain an accurate description of the vortex lines, the number of segments in the computation is continuously adjusted as the vortex filaments evolve in time. Finally, a representative noise level is injected in the initial conditions (corresponding to a 0.1% free-stream-turbulence level) to more fully simulate the experimental conditions and to trigger the appearance of instabilities.

As expected, the primary instability of the cylindrical interface consists of a strong rolling into a well-defined vortex ring. The wavelength of that rolling is being dictated by the modulation imposed on the circulation of the individual vortex rings, as shown in figure 10 (*a, b*). When the simulation is carried further in time, apart from the continued building-up of the main ring, the rings subject to the maximum shear – those shaping the jet at stations close to the already strong vortex ring – become strongly unstable. The distortion of each of these rings produces in it a marked difference in the updraught velocity that different parts of it experience. Kinks that fold inward see a much higher upward velocity and get vertically strained towards the main vortex ring. Folds that bend outward will be swept backwards by the relative velocity of the outer stream, as viewed in a convected frame of reference.

Figure 10 (*a*) shows an early stage in the simulation at $t\Delta U/R = \tau \approx 0.8$, where ΔU is the velocity difference between the two streams and R is the nozzle radius. Although not very different from the initial configuration, a barrel-like shape is forming caused by the spatial modulation of the circulation. As noted above, only the central excitation wavelength of the infinite sequence is displayed. Figure 10 (*b*) shows an advanced stage in the evolution of the rolling process ($\tau = 3.2$). The main vortex ring can be easily perceived by the entangling of high-circulation vortex lines. As can be seen, most of the vorticity initially shed in the flow gets concentrated in the main rings (§7 features quantitative measurements of the concentration of the circumferential vorticity into a big vortex ring and of the onset and growth of streamwise vorticity). Figure 10 (*c*) shows highlighted rings from figure 10 (*b*), in which the development of streamwise vorticity is evident as a consequence of the instability and deformation of the vortex rings placed at the location of maximum shear. When cut through a plane normal to the flow direction (the plane would be right to left in figure 10 *a–c*), the loops highlighted in figure 10 (*c*) will essentially provide a two-dimensional counter-rotating vortex pair, which produces the internal patterns shown in figure 3 by entraining the smoke present on the internal face of the main vortex ring. We also believe that there might be additional streamwise vortices in the external fluid entrained inside the jet; these are not displayed because there is no smoke to enable their visualization.

7. Quantitative results

The extraction of numerical values from flow-visualization data is a very attractive possibility since it can provide simultaneous maps of a flow parameter of interest over extended areas of the flow. This is useful for analysing the evolution of a fluid flow. However, when the purpose is to compare an analytical or numerical solution to the experimental results, we are faced sometimes with a multi-dimensional comparison task that cannot be performed easily. Furthermore, in turbulent flows it is customary to consider integral quantities such as characteristical lengths and times, but *instantaneous* point-to-point comparisons even between subsequent realizations of the same flow are often nearly impossible to make. To overcome these

problems, it is often desirable to be able to extract global quantities that summarize a certain aspect of the flow into a single value. An example of work in this area is the measurement of spreading rates in the mixing layer by Brown & Roshko 1974. More recently, starting from a computational data base, Moin & Kim 1985, produced statistics about the preferred orientation of vortex tubes in a simulated turbulent channel flow.

In the present study, we have focused our attention on two global quantitative measurements of relevant importance from the flow-visualization data. These are the *surface-to-volume* ratio and the *entrainment* of external fluid into the jet. Vorticity-distribution parameters are also extracted from the numerical computations.

The amount of surface, or interface between the two mixing streams, per unit volume of one of the species, is important because it gives both an estimate of the typical size of the small eddies in the dispersed material (the inner jet) and a prediction of the rate at which molecular mixing between the two streams may take place. A simple but properly done measurement procedure applied to figures 4 and 5 will produce for each of the forty available cross-sections values for the amount of smoke material and for the length of the edges that circumvent the smoke fluid. The ratio of these quantities corresponds to the surface-to-volume ratio in a two-dimensional approximation, where the structure is supposed to extend prismatically from one cross-section to the next one. The other possibility is to assume that the white volume, whose cross-sections are displayed in figure 2, are entirely isotropic and have no preferred dimension. In the first assumption, the surface-to-volume ratio is

$$\frac{S_{3D}}{V} = \frac{L_{2D}}{S_{2D}},$$

while in the isotropic assumption

$$\frac{S_{3D}}{V} = \frac{4}{\pi}\frac{L_{2D}}{S_{2D}},$$

where 2D subscripts denote quantities measured or estimated on a two-dimensional cross-section, and 3D denotes volume and surface in a general three-dimensional space. Since the evolution that takes place from one cross-section to the next is not very drastic (see figures 2–8) we believe that the two-dimensional approximation is more likely to be true in the present application. Figure 11 (a) shows the surface-to-volume ratio for all the slices in one wavelength of the rolling eddy versus the downstream position measured from the starting point of the rolling period and non-dimensionalized by the length of the structure (λ). The surface-to-volume ratio is essentially the inverse of the characteristic size of the planar structures shown in the cross-sections. The graph shows two different and distinct peaks. It is clear that the peak corresponding to low values of x/λ and therefore to the unrolled part of the jet represents the previously mentioned longitudinal structures and core of the jet, and the ratio value represents the typical size of these structures. Further downstream, there is another peak that corresponds to the vortex ring itself, and it occurs at a relative position $x/\lambda \approx 0.55$–0.75. Higher surface-to-volume ratios in the forebody show that the flow scales are finer on the average than those present at low values of x/λ.

There is a not very well-known result of Debye, Anderson & Brumberger (1957) connecting the surface-to-volume ratio of an isotropic sectioned sample (such as that
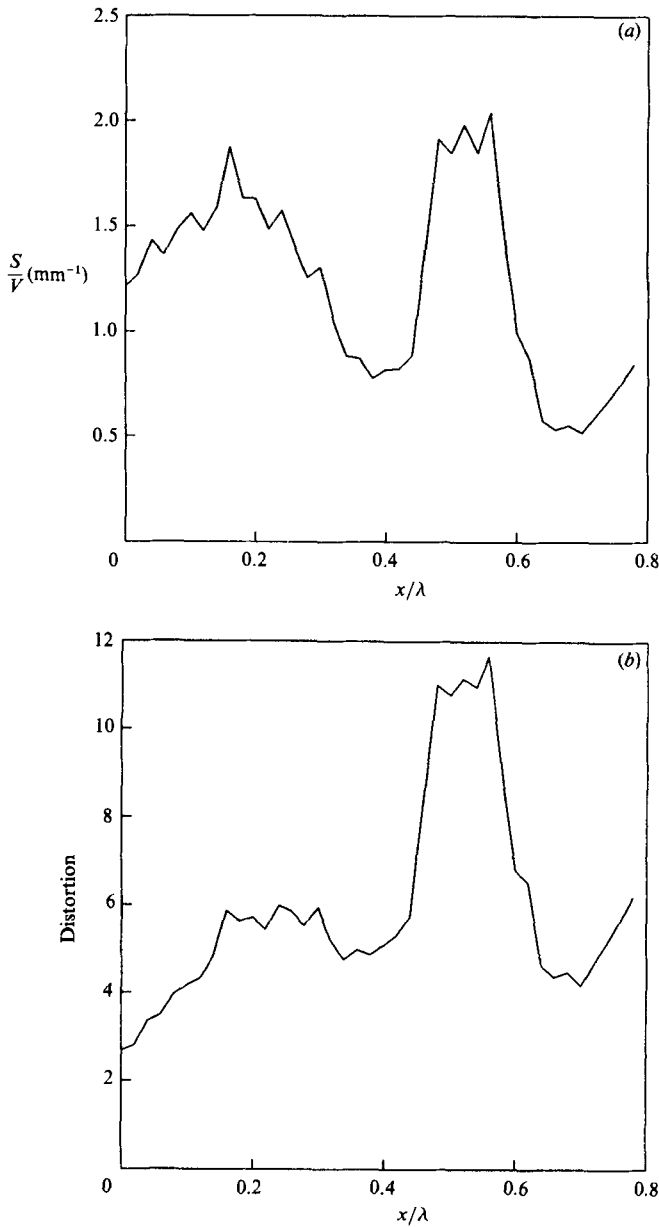
FIGURE 11. (a) Surface-to-volume ratio for the different cross-sections. (b) Distortion, $L/[2(\pi S)^{\frac{1}{2}}]$.

of gravel or any arid or bi-phase material) to the initial slope of the autocorrelation function. Debye *et al.* showed that†

$$\frac{S}{V} = -4(1-\phi)\,P'_{11}(0),$$

† It is necessary to warn that the volume considered here is the smoke volume, or that issued from the jet, whereas in Debye's article it is the whole volume. A void fraction makes up for the difference.
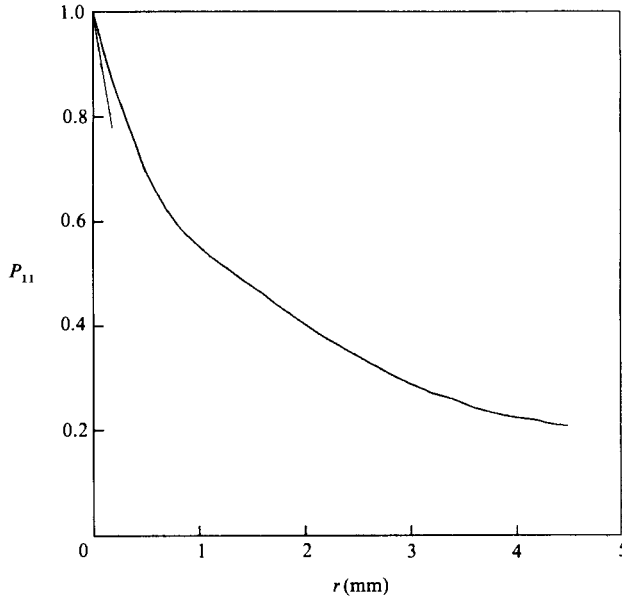
FIGURE 12. Autocorrelation function P_{11}.

where ϕ is the void fraction, or the ratio of non-smoke particles to smoke ones, and $P_{11}(r)$ is the probability that when randomly placing a segment of length r in the image such that one of its ends is lying on a smoke particle, the other end will fall on a smoke particle as well. Mathematically

$$P_{11}(r) = P[f(x+r) = 1 \,|\, f(x) = 1],$$

where the function $f(x)$ attains the value of one for a smoke particle and zero otherwise. Since we did accept a non-isotropic extension of the cross-sections in the longitudinal direction it is necessary to redo Debye's derivation on a planar basis. When this is carried out, the result is, as could perhaps have been guessed,

$$\frac{S}{V} = -\pi(1-\phi)\,P'_{11}(0).$$

Taking one of the cross-sections from figure 2 ($x/\lambda = 0.625$) the void fraction is 0.912, and from figure 12, $P'_{11}(0) \approx -0.075$ which yields a value of $S/V \approx 2.4$, which in turn compares very favourably with the values shown in figure 11(a).

The surface-to-volume ratio is also a dynamic quantity of interest in a flow and evolves in time from values initially determined by the large-scale geometry to values determined by the small-scale eddies in the Kolmogorov range. Broadwell & Breidenthal (1982) discussed a model for the temporal evolution of this ratio in a turbulent shear flow. Unfortunately, our data do not allow the unknown constant in their model to be estimated. To do that, measurements of the surface-to-volume ratio need to be carried out at two different evolution stages of the flow (i.e. two different positions downstream). This information is not available within a single wavelength of the instability of the coflowing jet since the rolling process tends to mix the degree of evolution within the structure and it is only possible to refer to an average evolution stage for the structure at each time and position.

There is an alternative way of dealing with the surface/volume data, namely by considering the ratio between the length of interface and the root of the area

contained within those edges. Since this is a non-dimensional variable, it is now independent of the total amount of smoke material present in any cross-section, and it merely expresses the level of distortion (somehow, the 'age' of that structure) of the flow. Figure 11 (*b*) contains the value of $L/S^{\frac{1}{2}}$ relative to that of a single circle of the same total area and it shows more clearly where the ageing produced by the vorticity has been more intense. Since the amount of material contained in low values of x/λ is small, the peak shown in figure 11 (*a*) disappears and only the one corresponding to the main vortex ring survives in an almost identical shape. We believe this second approach to be of perhaps greater interest, since it can possibly be connected to the onset of chaotic behaviour. The small scales present at low x/λ should not be taken as evidence of turbulence, since they result from the mass redistribution forced by entrainment into the main rolled-up body.

For interpretation of our results, it is important to consider the effects of sampling and digitization on the accuracy of the surface-to-volume ratio and entrainment. In this regard, we observe that the sampling interval is smaller than the Kolmogorov scale (about 0.3 mm) and that the resolution (0.09 mm/pixel) is sufficient to accurately describe geometrical parameters derived from the images. In particular, we have varied the sampling interval and noticed that even for lower-resolution images the $L/S^{\frac{1}{2}}$ ratio stays constant to within 10%, until the resolution is so coarse that the smallest scales (about 0.3 mm) are no longer resolved.

Figure 7 has given a qualitative idea about how much external fluid has been entrained inside the swollen body of the jet. The entrainment ratio is defined in various ways in the literature. Crow & Champagne (1971) define entrainment as the longitudinal derivative of the volume flux. Perry *et al.* (1980) give a definition of an entrainment velocity based on spatial growth ratios. In both cases, regardless of whether they provide numerical values or not, the common characteristic is that these are averaged values based on mean profiles or mean dividing streamlines. As noted by Broadwell & Breidenthal (1982) the presence of coherent structures in the flow (as is the case in the acoustically excited coflowing jet) may invalidate results concerning mixing of two species, since outside material incorporated into the jet is not necessarily mixed with the jet fluid in a short time. What can be measured from the data base consisting of the cross-sections like those in figure 2 is the relative amount of external (clear) flow that is almost completely surrounded by smoke fluid. It is clear that since we could resolve those particles as external fluid they have not yet been mixed with the smoke fluid. Taking only those sections for which the smoke-tagged fluid really closes over the dark regions ($x/\lambda \sim 0.375\text{–}0.975$) the ratio of the external fluid to the jet fluid comes up to a value of 0.83. Only a crude comparison can be made with the values measured by Crow & Champagne in a forced round jet. At $X/D \approx 3$ they measured values of Q/Q_e close to 1.6, where Q is the mass flux at the certain X/D and Q_e is the jet mass flux. Our value for the external–internal ratio will give $Q/Q_e \approx 1.83$, though taking into account the part of Q_e that is left outside the range of x/λ considered will probably lower our value. However, it is necessary to point out that the nature of the smoke-tagging procedure makes it impossible to say much about the external untagged fluid, and the values obtained by Crow & Champagne made use of mean profiles extending far away from the mixing region.

Although the numerical simulations presented in the previous section do provide additional details of the flow, several integrated quantities can be easily derived from the resulting data. The process of rolling-up – primary instability – can be quantified by measuring the accumulation of vorticity into a main vortex ring. Figure 13 (*a*)
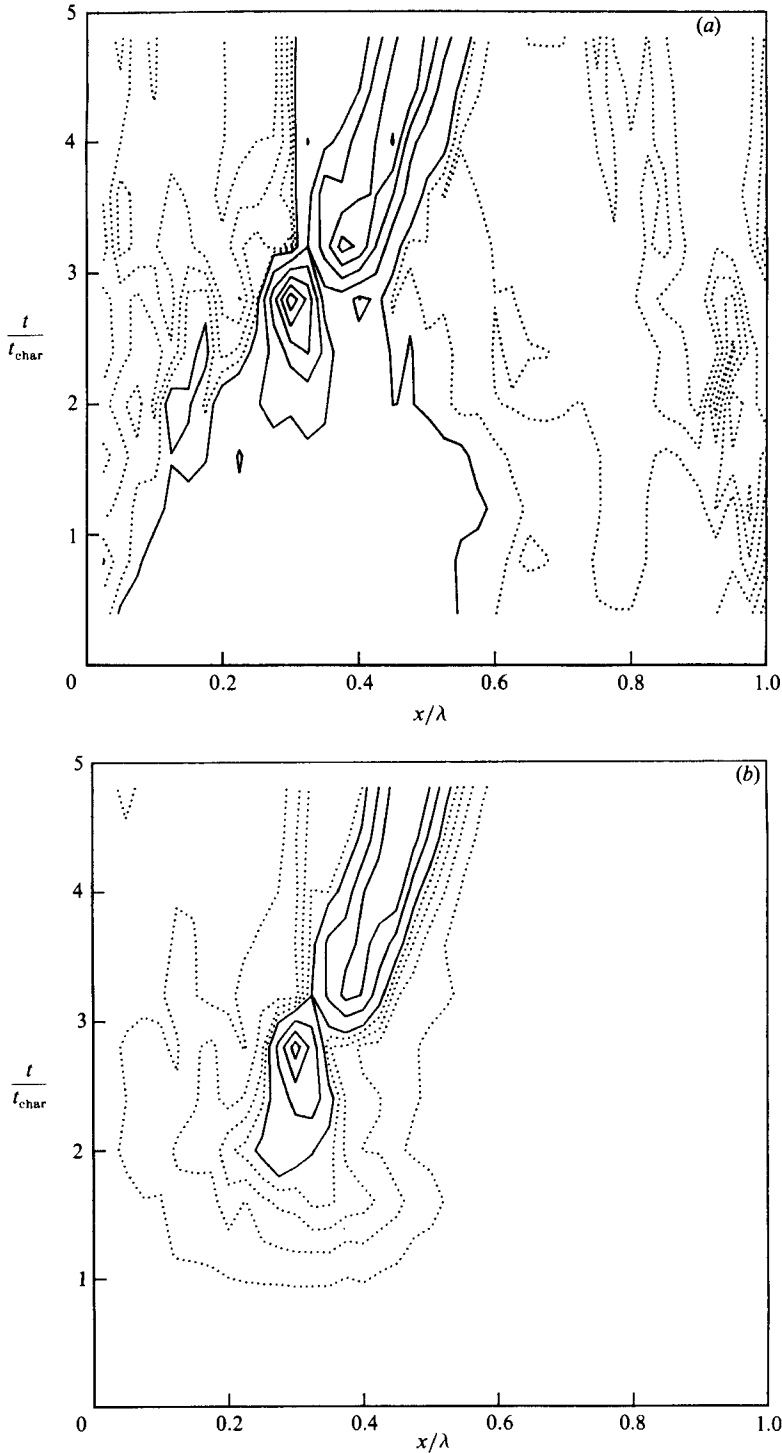
FIGURE 13. Vorticity distribution. Circulation per unit axial length divided by the total initial circulation at the same x/λ. (a) Absolute circulation normal to the mean flow direction: ———, circulation greater than unity, increment between lines $= 1$; ..., circulation less than unity, increment $= 0.2$. (b) Axial absolute-value circulation: ———, circulation greater than unity, increment $= 0.5$; ..., circulation less than unity, increment 0.2.
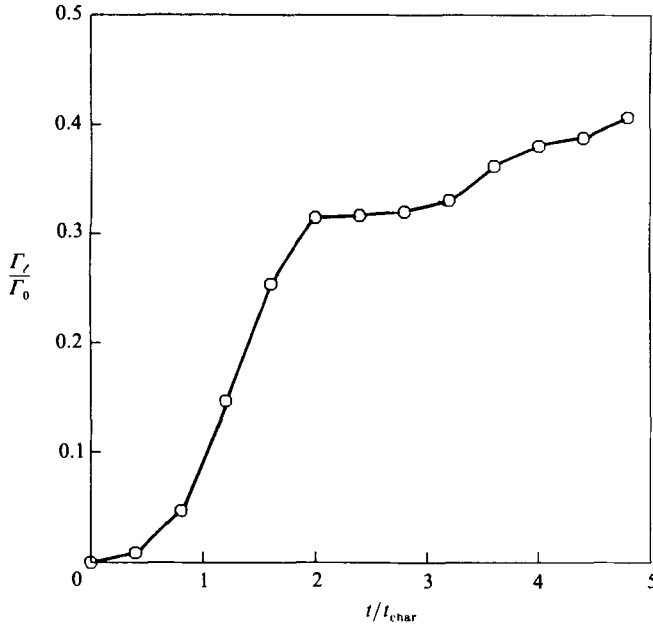
FIGURE 14. Time evolution of total absolute-value longitudinal circulation in the complete wave-length divided by the initial normal circulation.

shows the time evolution of the circumferential vorticity. This figure clearly shows how the vorticity concentrates into a single strong vortex ring and, after a certain time, it seems to spread somewhat. Analogously, the distribution and growth of streamwise circulation – secondary instability – can be followed in figure 13(b). Notice that, probably owing to slanting present in the main vortex ring, the component of vorticity projected in the axial direction can double the component of circumferential vorticity per unit axial length originally deposited at that position of x/λ. Figure 14 displays the variation of the total (absolute-value) streamwise circulation relative to the total initial circulation present in the flow. Besides noticing the high values that the longitudinal circulation can attain, it is worth mentioning the appearance of two different regimes, bounded by an inflexion in the development of streamwise vorticity. We have not yet found a reasonable explanation for this behaviour, but the reader may compare this with figure 13(a, b) to see that the flattening of the production in figure 14 occurs simultaneously with the appearance of the highest spatial concentrations of both circumferential and longitudinal vorticities, which shows the ripening in the formation of the big vortex ring. The same kind of behaviour regarding the growth of the main vortices has also been observed in the numerical simulation of the rolling-up of the time-developing mixing layer by Corcos & Sherman (1984).

A third instability is present in the experimental data. This is the one responsible for the appearance of the five longitudinal streamers. This is really an instability that develops in the longitudinal vorticity and corresponds, as mentioned above, to that predicted by Lin & Corcos (1984). In this respect, figure 10 (a–c) is 'honest', in the sense that no artificial excitation has been introduced into the flow simulation beyond those that are present in the real experiment. The noise induced in the initial condition is a pure white noise and so it excites all the circumferential wavenumbers alike. This may possibly be the reason why the simulations do not show a
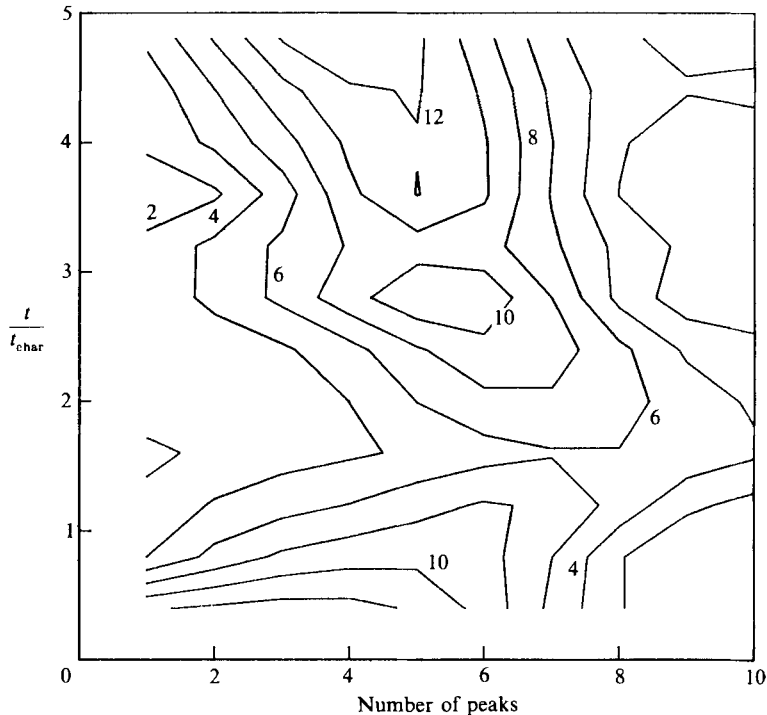
FIGURE 15. Time evolution of histogram of the number of rings containing a certain number of peaks over 1.0 r.m.s. of the vertical fluctuations.

circumferential instability of order five as clearly as the smoke pictures (figure 3). However, it is possible to quantify the typical number of peaks present in the flow at a certain time, and construct a histogram of the number of rings that contain a certain number of peaks. A peak is defined as a succession of two or more consecutive nodes, whose distance to the plane that best fits the ring is higher than σ, where σ is the r.m.s. value of the distances for all the nodes in the ring. The result is shown in figure 15 where the contour plot of the time-evolving histogram is presented. It can be seen that for small times, the lower number of peaks are predominant, while as time progresses, the higher range of peaks (4–7) becomes more active. After $\tau \approx 2$ it slowly drifts back towards smaller number of peaks. This is in qualitative agreement with the clear-cut five-fold instabilities present in the experimental data.

8. Holographic display

The information available in the data base pertaining to our fluid structure is much richer than can be displayed in any of the previous two-dimensional figures. This suggests that conventional display techniques are lagging in power behind data acquisition facilities. However, we believe that holographic methods are more powerful in the sense that the spatial density of information that they can store and simultaneously display is far greater than for conventional phase-lagging techniques. In an attempt to gather all the three-dimensional data of our flow, and to facilitate its comprehension, we have produced a holographic-display representation of the coflowing jet eddy. The procedure for generating multiplex holograms has been
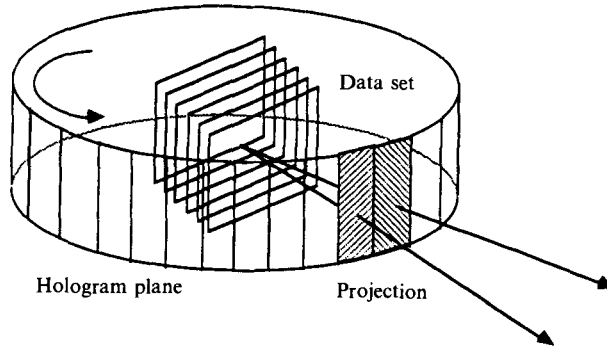
FIGURE 16. Source-attenuation model.

reported previously, by Hesselink *et al.* (1983), but will be briefly repeated here for the sake of completeness.

A computational procedure is used to determine views of the object as seen by an observer located some distance away from the object, which in our case is defined by data in a stack of cross-sections. The intensity of light propagating along rays which converge at the eyes of the observer is computed by considering each point in the object to act both as a source and as an attenuator. Each point along the lines, as drawn in figure 16, acts as a source of light and as an attenuator for light coming from points farther away from the observer. The net result of summing all these contributions is the intensity measured along each ray reaching the observer. In our particular case only the surface of the structure is displayed and the intensity of each voxel is computed using an illumination scheme as discussed in §4. Thus, only voxels at the surface are used to compute the projections. The collection of rays corresponding to a particular viewing position is called a projection and represents the view of the object as perceived by the observer from that direction. To generate a wide-field-of-view display system, projections are computed at $\frac{1}{3}°$ intervals for a 120° viewing angle.

Upon calculation of the projections a hologram is created by using an optical arrangement as shown in figure 17(a). Each computed projection is displayed on a flat CRT screen and recorded in sequence on a 16 mm movie, which results in 360 movie frames, each containing one projection. The images are recorded holographically using an anamorphic imaging system. A combination of a spherical and cylindrical lens is used to image the projection onto a narrow slit in front of holographic film. Simultaneously a reference beam is derived from the same laser and the interference between the projection and the reference beam (i.e. a hologram) is recorded on film; one strip hologram for each projection for a total of 360 holograms side by side. The hologram may at this point be viewed by wrapping the film around a cylinder for large-field-of-view displays or by placing it on a flat substrate and using a point light source as shown in figure 17(b); for this purpose a white light source may be used. The object appears to be present behind the film and can be viewed by an observer located on the other side of the hologram. The procedure described here creates distortions for large objects and large viewing angles; these distortions can be compensated for by properly modifying the data base before calculating the projections (Hesselink *et al.* 1983).

For the purpose of displaying the date in publishable form yet another transformation is needed. The hologram as described here is used as a master from
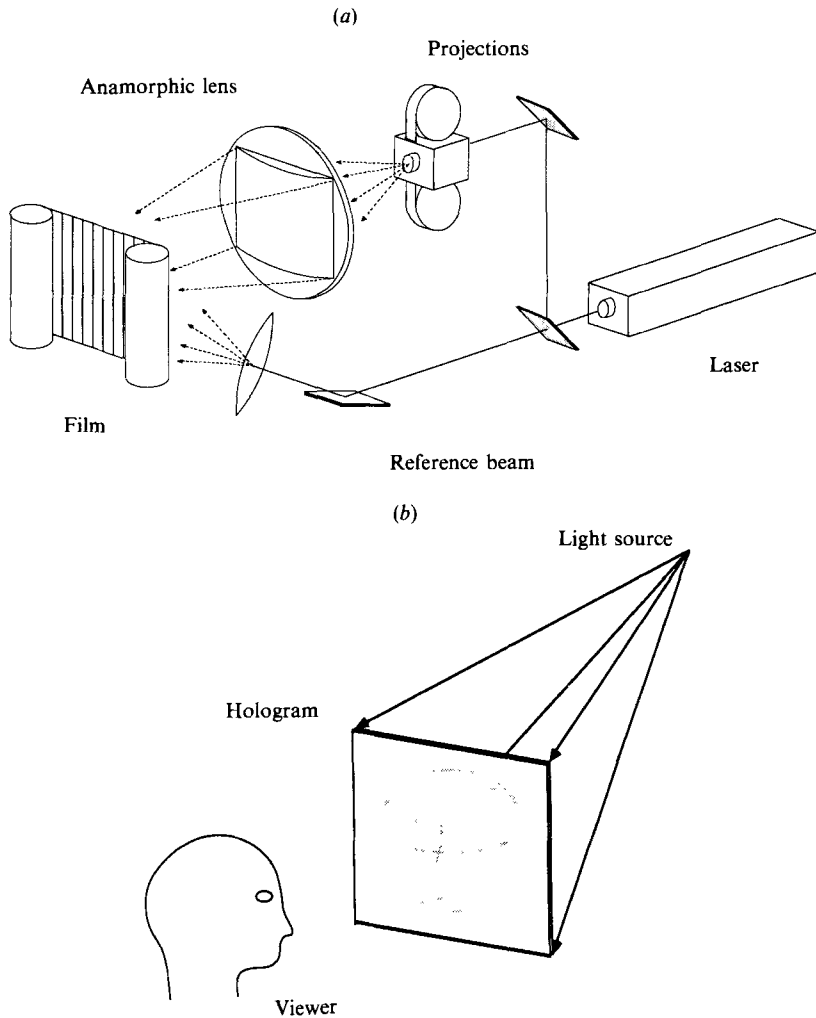
FIGURE 17. (a) Multiplex hologram construction. (b) Illumination scheme for hologram viewing.

which embossed or photopolymer copies are made using standard holographic techniques (Caulfield 1979). This procedure produces a reflection hologram in which the image is located relatively close to the hologram plane and often straddles it. Such a hologram can again be viewed using white light.

The result of the above process is displayed in the hologram contained in figure 18. Proper viewing of the hologram yields a black and white three-dimensional view of the coflowing jet eddy discussed in this paper. Many of the features noted in the two-dimensional projections are readily visible, with the increased three-dimensional sensation provided by the sideward parallax. The transition between consecutive cross-sections has been interpolated using the method of Wu & Hesselink (1988) in the case of the projections used for the hologram displayed.

Using this technique it is also possible to display time-varying three-dimensional objects in animated form. Besides displaying different views of the same static object, one can show a time sequence so that time is encoded in angular position. Thus it is possible to display four-dimensional data.
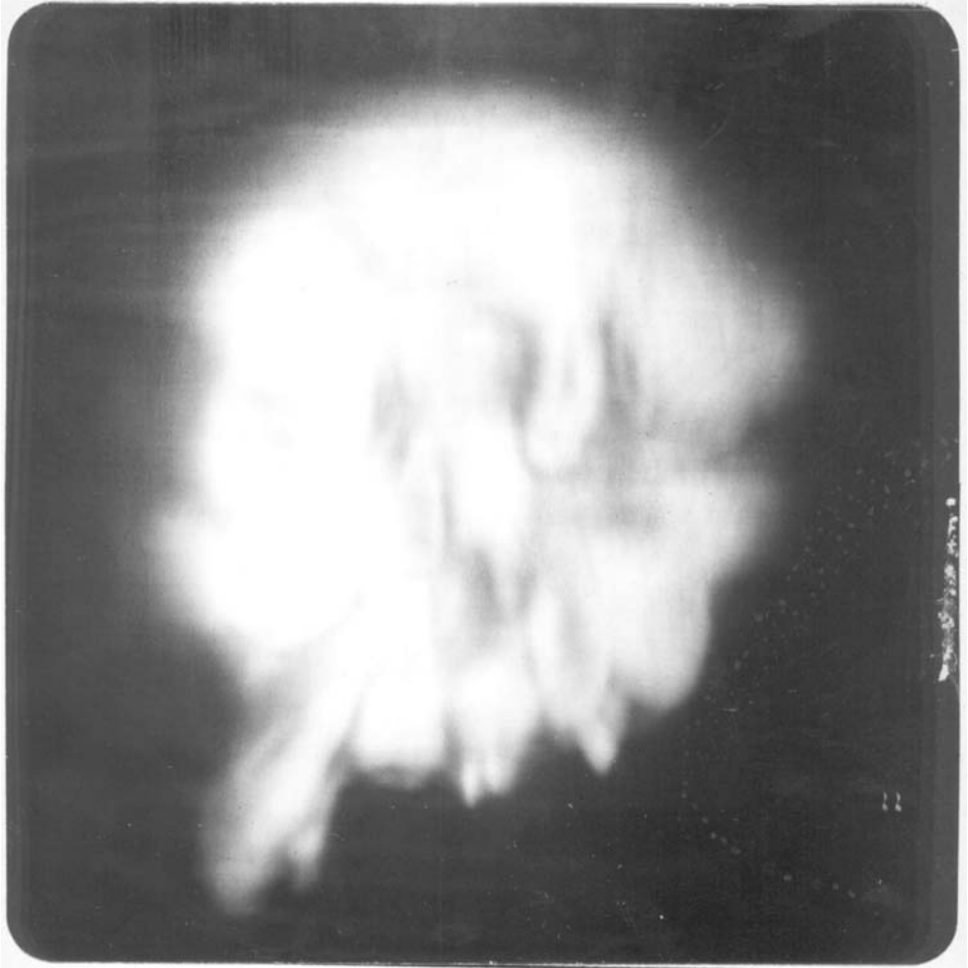
FIGURE 18. Holographic representation of a coflowing-jet eddy. The hologram of the eddy is synthesized from a set of views generated by the authors using the contour-surface reconstruction and rendering methods of Wu & Hesselink (1988). For best viewing, illuminate with a white light source of small size placed at 45° above the plane of the hologram. (© 1988 J. C. Agüí, K. Wu, and L. Hesselink, Stanford University.)

9. Conclusions

A computer-based, simple, yet powerful, method for reconstruction of three-dimensional flow structures is demonstrated. The method includes subsequent usage of image processing and three-dimensional graphics. Hidden-surfaces removal and lighting enhance the solid perception of the structure. The method appears to be a useful tool for topological analysis of complex structures. Surface-to-volume ratios and entrainment values can be derived from the three-dimensional data base. These values are discussed and compared with those published in the literature. A second approach to understanding the same flow has been pursued by using a vortex-element method. This method permits the description of the flow in terms of vorticity distribution. The numerical results confirm the hypothesis of a hierarchy of

three instabilities: rolling-up of the vorticity sheet into well-defined periodic vortex rings; creation of streamwise vorticity in the braids that connect the rings; and, last, the instability and grouping of this longitudinal vorticity into vortex tubes whose intensity increases owing to the strain produced by the main vortex ring. The mechanism is found to be similar to that present in the plane mixing layer.

Finally, a fully three-dimensional display of the images is achieved by means of a synthetic multiplex hologram.

REFERENCES

ASHURST, W. T. 1981 Vortex ring instability. *Bull. Am. Phys. Soc.* **26**, 1267.

BECKER, H. A. & MASSARO, T. A. 1968 Vortex evolution in a round jet. *J. Fluid Mech.* **31**, 435–438.

BROADWELL, J. E. & BREIDENTHAL, R. E. 1982 A simple model of mixing and chemical reaction in a turbulent shear layer. *J. Fluid Mech.* **125**, 397–410.

BROWN, G. L. & ROSHKO, A. 1974 On density effects and large structure in turbulent mixing layer. *J. Fluid Mech.* **64**, 775–816.

CANTWELL, B. J. 1981 Organized motion in turbulent flow. *Ann. Rev. Fluid Mech.* **13**, 457–515.

CAULFIELD, H. J. 1979 *Handbook of Optical Holography*. Academic.

CORCOS, G. M. & LIN, S. J. 1984 The mixing layer: deterministic models of a turbulent flow. Part 1. Introduction and the two-dimensional flow. *J. Fluid Mech.* **139**, 29.

CORCOS, G. M. & SHERMAN, F. S. 1984 The mixing layer: deterministic models of a turbulent flow. Part 2. The origin of the three-dimensional motion. *J. Fluid Mech.* **139**, 67.

CROW, S. C. & CHAMPAGNE, F. H. 1971 Orderly structure in jet turbulence. *J. Fluid Mech.* **48**, 547–591.

DEBYE, P., ANDERSON, H. R. & BRUMBERGER, H. 1957 Scattering by an inhomogeneous solid. II. The correlation function and its applications. *J. Appl. Phys.* **28**, 679–683.

FOLEY, J. D. 1983 *Fundamentals of Interactive Computer Graphics*. Addison-Wesley.

FUCHS, H., KEDEM, Z. M. & USELTON, S. P. 1977 Optimal reconstructions from planar contours. *Commun. ACM* **20**, 693–702.

GONZALEZ, R. C. 1987 *Digital Image Processing*. Addison-Wesley.

HESSELINK, L. & HELMAN, J. 1987 Evaluation of flow topology from numerical data. *AIAA Invited Paper*: 87-1181-CP.

HESSELINK, L., PENDER, J., JAFFEY, S. M. & DUTTA, K. 1983 Quantitative three-dimensional flow visualization. In *Proc. 3rd Intl Symp. on Flow Visualization, Ann Arbor, Michigan*. Hemisphere.

HUSSAIN, A. K. M. F. & CLARK, A. R. 1981 On the coherent structure of the axisymmetric mixing layer: a flow visualization study. *J. Fluid Mech.* **104**, 263–294.

JIMÉNEZ, J. 1985 Some computational problems in computer-assisted flow visualization. *Intl Symp. Comp. Fluid Dynamics. Tokyo. Sept. 9–12.*

JIMÉNEZ, J., COGOLLOS, M. & BERNAL, L. P. 1985 A perspective view of the plane mixing layer. *J. Fluid Mech.* **152**, 125–143.

LAU, J. C. & FISHER, M. J. 1975 The vortex-street structure of 'turbulent' jets. Part 1. *J. Fluid Mech.* **67**, 299–337.

LEONARD, A. 1975 Numerical simulation of interacting, three-dimensional vortex filaments. In *Proc. Intl Conf. Numer. Meth. Fluid Dyn. 4th. Colo.* pp. 245–250. Springer.

LEONARD, A. 1985 Computing three dimensional incompressible flows with vortex elements. *Ann. Rev. Fluid Mech.* **17**, 523–559.

LIN, S. J. & CORCOS, G. M. 1984 The mixing layer: deterministic models of a turbulent flow. Part 3. The effect of plane strain in the dynamics of streamwise vortices. *J. Fluid Mech.* **141**, 139–178.

MOORE, D. W. & SAFFMAN, P. G. 1972 The motion of a vortex filament with axial flow. *Phil. Trans. R. Soc. Lond.* A **272**, 403–429

MOIN, P. & KIM, J. 1985 The structure of the vorticity field in a turbulent channel flow. Part 1. Analysis of instantaneous fields and statistical correlations. *J. Fluid Mech.* **155**, 441–464.

NEWMAN, W. M. & SPROULL, R. F. 1979 *Principles of Interactive Computer Graphics*. McGraw-Hill.

PERRY, A. E., LIM, T. T. & CHONG, M. S. 1980 The instantaneous velocity fields of coherent structures in coflowing jets and wakes. *J. Fluid Mech.* **101**, 243–256.

PRATT, W. K. (ed.) 1978 *Digital Image Processing*. Wiley-Interscience.

STRAWA, A. W. & CANTWELL, B. 1985 Visualization of the structure of a pulsed methane–air diffusion flame. *Phys. Fluids* **28**, 2317–2320.

WIDNALL, S. E. 1975 The structure and dynamics of vortex filaments. *Ann. Rev. Fluid. Mech.* **7**, 141.

WU, K. & HESSELINK, L. 1988 Computer display of reconstructed 3-D scalar data. *Appl. Optics* **27**, 2.